Grüneisen rule in cubic rare-earth cage systems: the examples of LaB6 and LaPt4Ge12

Mehdi Amara, Christine Opagiste, Natalya Yu Shitsevalova

Journal of Physics:
Condensed Matter

Grüneisen rule in cubic rare-earth cage systems: the examples of LaB_6 and $LaPt_4Ge_{12}$

OPEN ACCESS
IOP Publishing
Journal of Physics: Condensed Matter
J. Phys.: Condens. Matter **37** (2025) 205404 (13pp)
https://doi.org/10.1088/1361-648X/adcbfb

Grüneisen rule in cubic rare-earth cage systems: the examples of LaB_6 and $LaPt_4Ge_{12}$

Mehdi Amara[1,*], **Christine Opagiste**[1] **and Natalya Yu Shitsevalova**[2]

[1] Institut Néel, Univ. Grenoble Alpes, CNRS, Grenoble INP (Institute of Engineering Univ., Grenoble Alpes), 38000 Grenoble, France
[2] Frantsevich Institute for Problems of Materials Science, National Academy of Sciences of Ukraine, Kyiv 03680, Ukraine

E-mail: mehdi.amara@neel.cnrs.fr

Received 2 December 2024, revised 2 April 2025
Accepted for publication 11 April 2025
Published 24 April 2025

Abstract

Specific heat and thermal expansion properties are investigated in two non-magnetic rare-earth cage compounds, LaB_6 and $LaPt_4Ge_{12}$, which represent extremes in guest-to-cage mass ratio. Using simplified phonons dispersions for the two lowest branches, a theoretical framework is proposed for the low temperature thermodynamic analysis of cage compounds. Within the quasi-harmonic approximation, the Grüneisen rule is found to break down even at low temperatures. However, under the influence of the flattened branches, it should be approximatively restored at intermediates temperatures. The model accurately describes LaB_6 specific heat below 50 K. In the $LaPt_4Ge_{12}$ case, the description is rapidly inadequate with increasing the temperature, which points to the interference of additional low frequency phonon branches. Subsequently, thermal expansion measurements are used to investigate the Grüneisen rule in these two compounds. As predicted, there appears to be distincts Grüneisen regimes at low temperature. This study will help distinguish between phonon and magnetic contributions to the thermal expansion in the RB_6 and RPt_4Ge_{12} series.

Keywords: Grüneisen, cubic, rare-earth, cages, LaB_6, $LaPt_4Ge_{12}$

1. Introduction

Cage compounds are characterised by a crystallographic structure in which tightly bonded atoms surround a larger element [1]. Inside this 'cage,' the guest atom has significant freedom of movement, a phenomenon often referred to as 'rattling'. These supposedly local modes were expected to reduce the thermal conductivity, which motivated the search, among cage systems, of materials with improved thermoelectric efficiency [2]. Some cage compounds can accommodate a magnetic ion inside the cage, which grants the system additional displacement degrees of freedom, alongside those of the ion spin and orbit. How these degrees of freedom cooperate, resulting in specific static and dynamic properties, as well as new kind of ordering processes, remains a largely unexplored field of investigation.

As demonstrated by the analysis of the antiferromagnetism in the rare-earth hexaborides series (RB_6, structure represented on figure 1), displacements inside the cage may play an essential role in the magnetically ordered states. In GdB_6, TbB_6 and PrB_6 [3–5], x-ray diffraction experiments show that, concomitantly with the antiferromagnetic order, static displacements waves of the rare-earth guest are stabilized. Indeed, the rare-earth displacements can minimize the exchange energy [3] for specific magnetic wave vectors, among which $\langle \frac{1}{4}\ \frac{1}{4}\ \frac{1}{2} \rangle$, recurrent in the RB_6 series. In rare-earth hexaborides, the cage context is then active in the definition of the magnetic wave vector

* Author to whom any correspondence should be addressed.

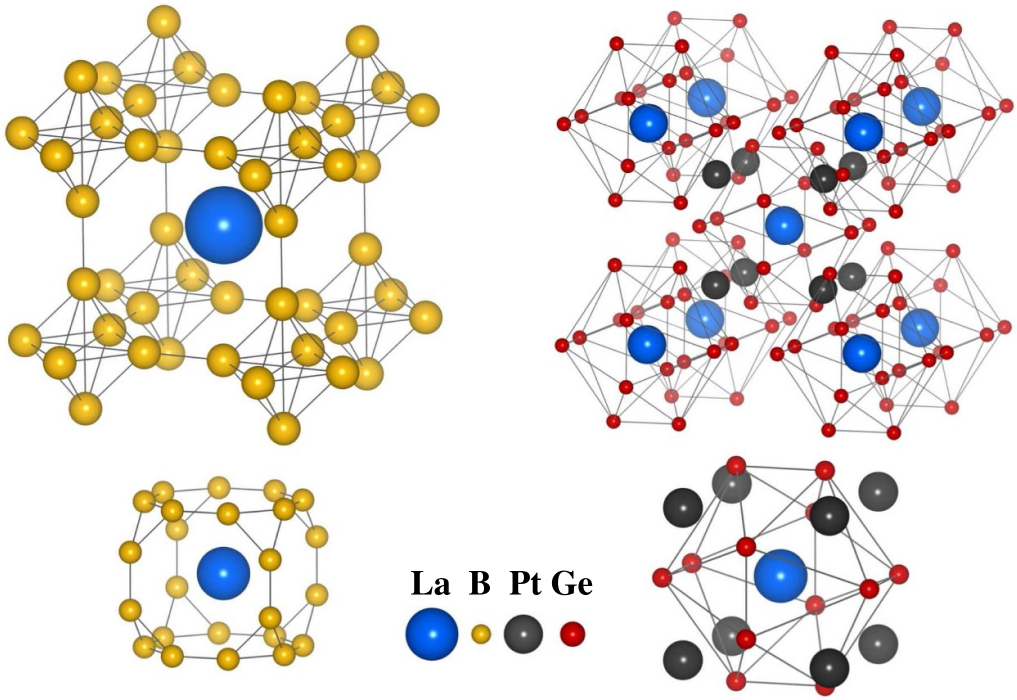

Figure 1. Left: Sketch of the simple cubic structure of LaB_6, with the boron cage enclosing the La^{3+} ion shown below. Right: body-centered cubic structure of the filled skutterudite $LaPt_4Ge_{12}$, with the Pt_4Ge_{12} cage surrounding the La^{3+} ion detailed below. Images generated using the VESTA software.

and, moreover, determines the first-order nature of the magnetic transition.

Another distinctive feature of the cage environment arises from the crystalline electric field (CEF). In the paramagnetic state, the static energy scheme of the 4*f* electrons is shaped by the CEF, reflecting the anisotropy of the lanthanide ion environment. This anisotropy should be consistent with the point symmetry at the rare-earth site. However, inside the cage, this symmetry applies only on average, as the rare-earth ion can depart significantly from its central position. Consequently, CEF schemes that would exhibit, at the cage center, an extra degeneracy relative to the Kramers minimum, acquire a dynamic width [6]. At temperatures close or below the energy width of a non-Kramers CEF ground-state, one can predict a reduction in the magnetic entropy and of the ionic susceptibilities, as well as a broader distribution of the rare-earth ion within the cage. This change in the distribution should affect the system's volume, resulting in a thermal expansion anomaly. To investigate these effects, one has to first determine the thermal expansion in absence of magnetic contributions. In rare-earth compounds, the non-magnetic contributions are typically evaluated by measuring a non-magnetic element in the series, such as the lanthanum (better suited to the light rare-earth series) or yttrium (for the heavier elements) based ones. Some modelling is then required to adapt the non-magnetic background to a particular magnetic element. For instance, in the case of specific heat measurements, one can take advantage of the Debye model for, via a mass correction, adjusting the phonons contribution to the magnetic elements. In the case of rare-earth hexaborides, the Debye approach cannot cope with the specificity of the cage compound, in particular the low energy, flattened, phonon branches. In [7], we proposed a two-frequency model, that accounts for the two lowest phonon branches, for deriving the non-magnetic background of CeB_6 from the LaB_6 specific heat data. In the present work, we extend this model within the quasi-harmonic approximation to describe the phonon contribution to thermal expansion. This approach allows us to define distinct temperature ranges in which an adapted form of the Grüneisen rule [8], specific to cage compounds, may apply. Within this framework, specific heat and thermal expansion measurements of LaB_6 are then analysed.

In addition to this investigation of a non-magnetic rare-earth hexaboride, the same approach is applied to the non-magnetic filled skutterudite compound $LaPt_4Ge_{12}$ [9, 10]. This is a distinct type of rare-earth cage compound, crystallizing in the body-centered cubic $LaFe_4P_{12}$-type structure [11] (see right side of figure 1), unlike the primitive cubic lattice of rare-earth hexaborides. The most significant difference from LaB_6, that affects the dynamic properties, is the guest-to-cage mass ratio, characteristic of a heavy guest in LaB_6 against a heavy cage for $LaPt_4Ge_{12}$. Rare-earth filled skutterudites exhibit a range of intriguing properties, such as the heavy-fermion and superconducting characteristics of $PrOs_4Sb_{12}$ [12], the metal–insulator transition in $PrRu_4P_{12}$ [13] and the non-magnetic ordering of $PrFe_4P_{12}$ [14]. The focus is here restricted to the specific heat and thermal expansion properties of $LaPt_4Ge_{12}$, which are confronted with the

two-frequency phonons model and discussed in relation to the LaB_6 cage compound paradigm.

2. Quasi harmonic model of the thermal expansion in cage systems

2.1. Phonons for a cubic lattice of cages

Describing phonons in a lattice of cages using the Debye approximation has limitations due to the influence of quasi-local modes. On the other hand, the purely local Einstein model does not accurately fit the specific heat data. These difficulties inspired a hybrid approach that combines both models [15]. In [7] we proposed a more realistic description, restricted to the two lowest phonon branches, that takes advantage of simplified dispersion relations. This stems from the observation in LaB_6 of similar dispersion curves for different polarizations and along different reciprocal space directions [16]. Similar traits are observed in filled skuterrudites [17, 18]. This model was developed for the primitive cubic lattice of the RB_6 series and needs to be extended to the body centered cubic lattice of the filled skuterrudites RPt_4Ge_{12}. In both cases, the crystal is envisaged as a lattice of rigid, but elastically coupled cages of mass M, each enclosing a guest of mass m. In the cubic context, the harmonic approximation implies an isotropic potential well, with a natural frequency ω_0 for the guest vibration in its cage. Considering a family of lattice planes, with spacing d, perpendicular to a unitary $\mathbf{u}$ vector, the classical equations of motion for a vibration mode with wave vector $\mathbf{q} = q\,\mathbf{u} = [q_x, q_y, q_z]$ (the reciprocal components are dimensionless, the indices x, y and z referring to the cubic axes of the reciprocal lattice), polarization s and frequency $\omega_s(\mathbf{q})$ yield the relation:

$$\cos\left(\frac{2\pi}{a}qd\right) = 1 - 2\left(1 + \frac{m}{M}\frac{{\omega_0}^2}{{\omega_0}^2 - {\omega_s(\mathbf{q})}^2}\right)\frac{{\omega_s(\mathbf{q})}^2}{{\Omega_s(B)}^2} \quad (1)$$

where a is the cubic lattice parameter, $\Omega_s(B)$ is, for the s polarization, the acoustic frequency for a lattice of empty cages (i.e. for $m = 0$) at the border zone point B in the $\mathbf{u}$ direction. The spacing d can be related to the reciprocal lattice vector $\mathbf{\Gamma B}$, where Γ is the origin: $d = a/2|\mathbf{\Gamma B}|$. It is convenient to introduce reduced frequencies as proportions of the guest frequency ω_0:

$$y_s(\mathbf{q}) = \frac{\omega_s(\mathbf{q})}{\omega_0} \text{and } Y_s(B) = \frac{\Omega_s(B)}{\omega_0}.$$

Equation (1) then reads as:

$$\cos\left(\pi\frac{q}{|\mathbf{\Gamma B}|}\right) = 1 - \frac{2}{{Y_s(B)}^2}\left(1 + \frac{\rho}{1 - {y_s(\mathbf{q})}^2}\right){y_s(\mathbf{q})}^2 \quad (2)$$

where $\rho = m/M$ is the guest/cage mass ratio. This form allows to immediately identify the frequencies at the origin of the Brillouin zone, where $\cos(\pi\frac{q}{|\mathbf{\Gamma B}|}) = 1$. In addition to the zero frequency of the acoustic branch, one gets the optical frequency at the origin:

$$y_s^o(\mathbf{0}) = \sqrt{1+\rho} \text{or } \omega_s^o(\mathbf{0}) = \omega_0\sqrt{1+\rho}.$$

This mode is the closest to the rattler picture and, for a guest in an isotropic harmonic well, is indifferent to the polarization. Along $\mathbf{\Gamma B}$, from equation (2) and introducing the function:

$$c_s(\mathbf{q}) = {Y_s(B)}^2\frac{1 - \cos\left(\pi\frac{q}{|\mathbf{\Gamma B}|}\right)}{2}, \quad (3)$$

one can define the two lowest phonon branches for an s polarization:

- Acoustic:

$$y_s^{\mathrm{a}}(\mathbf{q}) = \sqrt{\frac{1+\rho+c_s(\mathbf{q}) - \sqrt{(1+\rho+c_s(\mathbf{q}))^2 - 4c_s(\mathbf{q})}}{2}} \quad (4)$$

- Optic:

$$y_s^{\mathrm{o}}(\mathbf{q}) = \sqrt{\frac{1+\rho+c_s(\mathbf{q}) + \sqrt{(1+\rho+c_s(\mathbf{q}))^2 - 4c_s(\mathbf{q})}}{2}}. \quad (5)$$

These two branches materialize the avoided crossing between the flat mode at ω_0 and the acoustic branch of a lattice of empty cages with upper frequency Ω_0. This results in features characteristic of a cage system, as illustrated by the examples (a), (b) and (c) in figure 2:

- an acoustic branch that flattens close to ω_0, with an associated peak in the density of states. This effect is more pronounced for a light guest (small ρ) and hard lattice of cages, as in the case (b) of figure 2.
- the optical branch that starts at $\omega_s^{\mathrm{o}}(\mathbf{0}) = \omega_0\sqrt{1+\rho}$, separated from the acoustic one by a gap that increases with the ρ inertia ratio (see the differences in the examples of figure 2).

In the model used, these traits are common to all wave vector directions and phonon polarizations, with quantitative differences arising only from variations in the $Y_s(B)$ value. This allows a further simplification of the model, wherein the value of $Y_s(B)$, specific to a zone border point and polarization, is replaced by a unique, averaged Y_0 value. Accordingly, the function $c_s(\mathbf{q})$ is replaced by $c_0(\mathbf{q})$, independent of the polarization. Phonon related properties, arising from a sum over all modes inside the first Brillouin zone, then depend on only two frequency parameters: ω_0 and $\Omega_0 = \omega_0\,Y_0$. In some instances, the rattler frequency can be independently determined from spectroscopic techniques (such as neutron or infrared spectroscopy; see [16] for the LaB_6 example), which leaves Ω_0 as the only parameter to be adjusted.

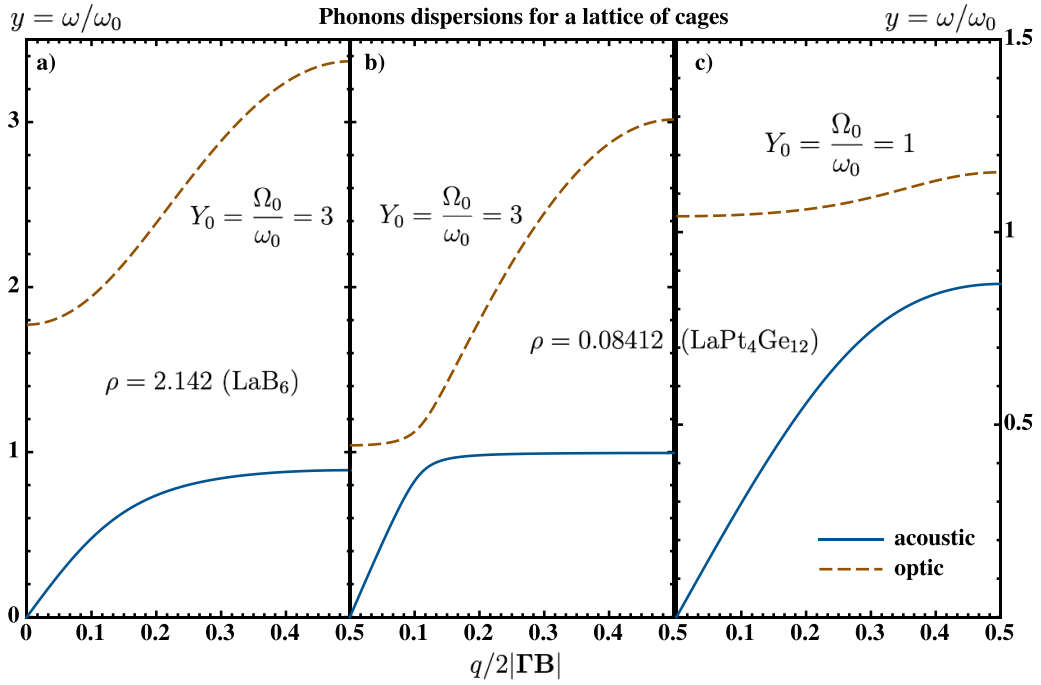

Figure 2. Three examples of generic dispersion curves for the lowest branches of a lattice of cages, showing the reduced frequency $y = \omega/\omega_0$ as a function of the wave vector along a first Brillouin zone segment $\mathbf{\Gamma B}$. (a) Heavy guest ($\rho > 1$), hard lattice ($Y_0 = 3$) case, here for the ρ mass ratio of LaB_6. (b) Light guest, hard lattice case for the mass ratio of $LaPt_4Ge_{12}$, keeping $Y_0 = 3$. (c) Light guest, softer lattice ($Y_0 = 1$), for the mass ratio of $LaPt_4Ge_{12}$, using a different vertical scale.

2.2. Calculation over the first Brillouin zone

Using the simplified dispersion functions, computing the specific heat, for instance, requires proper sampling of the Brillouin zone. Thanks to the cubic symmetry, one can restrict to samples evenly distributed within a representative volume of the first Brillouin zone. Figure 3 shows the tetrahedra enclosing such volumes in the case of a primitive cubic lattice (left, cubic P, that applies for LaB_6) and in the case of a centered cubic lattice (right, cubic I, for $LaPt_4Ge_{12}$). The border of the zone is the triangle XRM for the P case, respectively HPN for the I case. At points belonging to these triangles, the argument of the cosine $\cos(\pi \frac{q}{|\mathbf{\Gamma B}|})$ in equations (2) and (3) has to reach π. As these triangles are, respectively, perpendicular to $\mathbf{\Gamma X} = \left[\frac{1}{2}, 0, 0\right]$ and to $\mathbf{\Gamma N} = \left[\frac{1}{2}, \frac{1}{2}, 0\right]$, for a wave vector $\mathbf{q} = [q_x, q_y, q_z]$ inside the tetrahedra, one can rewrite the function $c_0(\mathbf{q})$, that replaces $c_s(\mathbf{q})$ in equations (4) and (5), as:

- Cubic P:

$$c_0(\mathbf{q}) = \frac{{Y_0}^2}{2}\left[1 - \cos\left(\pi \frac{\mathbf{q}\cdot\mathbf{\Gamma X}}{\Gamma X^2}\right)\right] = \frac{{Y_0}^2}{2}\left[1 - \cos(2\pi q_x)\right]$$

- Cubic I:

$$c_0(\mathbf{q}) = \frac{{Y_0}^2}{2}\left[1 - \cos\left(\pi \frac{\mathbf{q}\cdot\mathbf{\Gamma N}}{\Gamma N^2}\right)\right] = \frac{{Y_0}^2}{2}\left[1 - \cos\left[\pi\left(q_x + q_y\right)\right]\right]$$

Once defined a collection of N samples in the representative tetrahedron, these expressions allow for an easy implementation of the numerical calculation. For instance, a value for the phonons specific heat per unit volume is computed as:

$$C_{\mathrm{ph}}(T) = \frac{3k_{\mathrm{B}}}{V}\sum_{i=1}^{N}\sum_{\mu=(a,o)}\left(\frac{\hbar\omega_\mu(\mathbf{q}_i)}{k_{\mathrm{B}}T}\right)^2 \frac{e^{-\frac{\hbar\omega_\mu(\mathbf{q}_i)}{k_{\mathrm{B}}T}}}{\left(1 - e^{-\frac{\hbar\omega_\mu(\mathbf{q}_i)}{k_{\mathrm{B}}T}}\right)^2} \tag{6}$$

where V is the real space volume in correspondance with the N reciprocal sample vectors. The factor 3 accounts for the 3 polarizations and the index μ in the second summation refers to the phonons branches: the acoustic one (ω_{a}) and the lowest optical (ω_{o}) one. The $\omega_\mu(\mathbf{q})$ frequencies are obtained from equations (4) and (5), where, in place of $c_s(\mathbf{q})$, the generalized $c_0(\mathbf{q})$ function is used and values for ω_0 and Y_0 have been fixed. Note that, for the considered cubic lattices, the conventional cell with lattice parameter a contains $n = 1$ cage (simple cubic) or $n = 2$ cages (body centered cubic), which implies $V = Na^3/n$. To express the specific heat in $\mathrm{J\,(K\cdot\,mol)^{-1}}$ unit, the factor preceding the sum in equation (6) has to be replaced with $3R/N$, where R is the ideal gas constant. This approach was shown to be effective in the description of the phonons specific heat of LaB_6 and was subsequently used in the analysis of CeB_6 magnetic entropy [7].

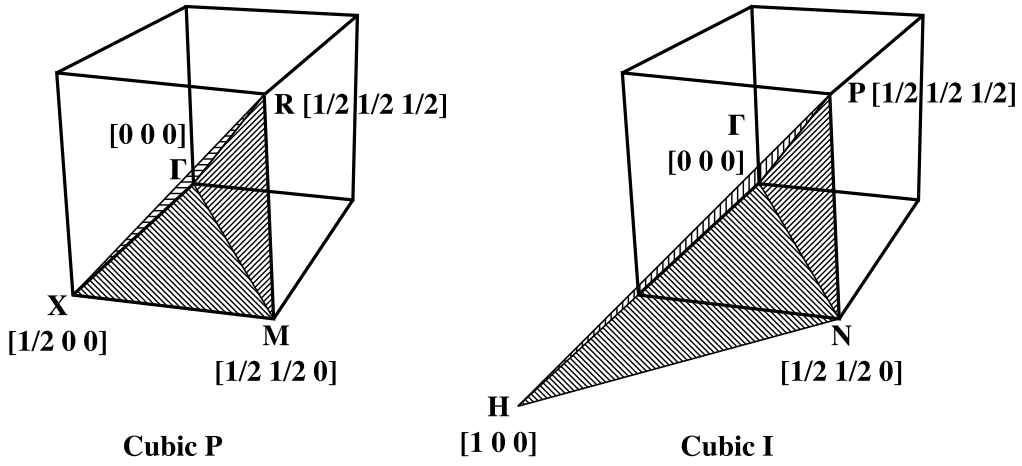

Figure 3. Representative tetrahedra of the first Brillouin zone: left for a primitive cubic lattice (RB_6 case), right for a centered cubic lattice (filled skuterrudite case). Integrals over the first BZ volume can be approximated by a discrete sum of evenly distributed samples in these volumes.

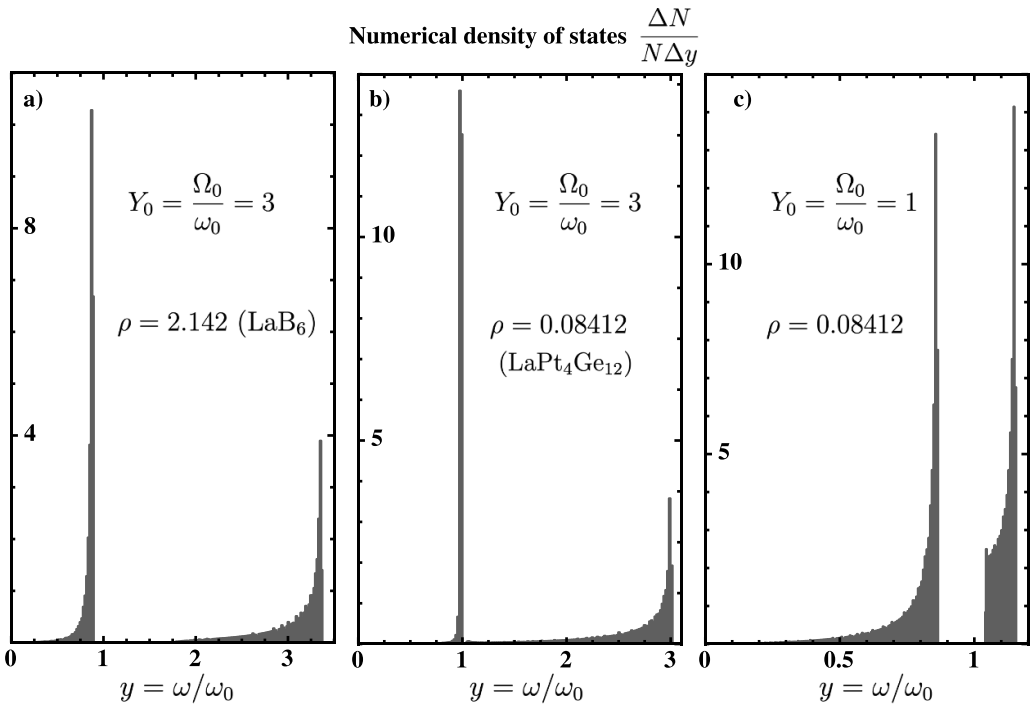

Figure 4. Numerical phonon densities of states plotted as function of the reduced frequency $y = \omega/\omega_0$, for the same examples as in figure 2. (a) Heavy guest ($\rho > 1$), hard lattice ($Y_0 = 3$) case, the ρ mass ratio of LaB_6 and a simple cubic lattice of cages. (b) Light guest, hard lattice case for the mass ratio of $LaPt_4Ge_{12}$, $Y_0 = 3$ and a body centered lattice. (c) Light guest, softer lattice ($Y_0 = 1$), for the mass ratio and body centered lattice of $LaPt_4Ge_{12}$.

Using the set of N evenly distributed samples in the representative volume, a spectral analysis can be performed: i.e. extracting from this set the distribution in energy of the phonons. This involves counting the number of samples ΔN inside energy intervals of fixed width Δy, where y is the energy in ω_0 unit. If N is large enough, this discrete approximation provides a good representation of what the continuous distribution would look like. Figure 4 shows these numerical energy distributions, for an energy range split into a 100 intervals, for the three dispersion cases shown in figure 2:

- case *a*), for frequency and mass ratios inspired by the LaB_6 example of heavy guest atoms inside a rigid lattice of cages. The distribution is computed for a set of $\approx 6 \cdot 10^5$ samples in the representative volume and shows features of both Debye and Einstein models. The increasing density of acoustic phonons, typical of the Debye model, is followed by a flattening of the acoustic branch, which results in a distinct Einstein-like peak. The heavy guests results in a large separation with the optical branch, this latter having negligible influence at low temperature.

- case b), based on the mass ratio of $LaPt_4Ge_{12}$ (i.e. in relative terms, a light guest atom) and considering a rigid lattice of cages. Computed for $\approx 1.2 \cdot 10^6$ samples in the representative volume, with its dominant peak, this distribution is the closest to the Einstein approximation. This features results from a small gap, with the acoustic and optical branches flattening at similar energies.
- case c), for the same $LaPt_4Ge_{12}$ mass ratio, but considering a softer lattice of cages. Computed for $\approx 1.2 \cdot 10^6$ samples in the representative volume, this distribution exhibits a more pronounced Debye character. However, due to the small gap and soft lattice, the flattened optical branch also contributes to the specific heat at intermediate temperatures. It is worth noting that this type of distribution resembles spectra obtained from inelastic neutron scattering on polycrystalline $LaPt_4Ge_{12}$. In [19], the low-energy region of the spectra shows a first peak at approximately 7.5 meV, then a second peak at 12.5 meV. This second peak is preceded by a shoulder around 10.5 meV, which matches the shape of the optical branch density for case c).

2.3. Phonon pressure

The same two branches model should apply for computing the low temperature phonon contribution to the thermal expansion. The approach here used is the quasi-harmonic one, where the harmonic treatment of the phonons is corrected for slight variations of the phonons frequency as function of the volume (see, for instance, [20]). One starts from the phonon contribution to the internal energy for a system of volume V, equivalent to N reciprocal lattice points:

$$U_{\mathrm{ph}}(T,V) = \frac{3}{2}\sum_{i=1}^{N}\sum_{\mu=(a,o)}\hbar\omega_\mu(\mathbf{q}_i) + 3\sum_{i=1}^{N}\sum_{\mu=(a,o)}\frac{\hbar\omega_\mu(\mathbf{q}_i)}{\mathrm{e}^{\frac{\hbar\omega_\mu(\mathbf{q}_i)}{k_B T}}-1}. \tag{7}$$

From the phonon internal energy, one has to derive the free energy: $F_{\mathrm{ph}}(T,V) = U_{\mathrm{ph}}(T,V) - TS_{\mathrm{ph}}(T,V)$. This in order to introduce the phonon pressure:

$$P_{\mathrm{ph}}(T,V) = -\left.\frac{\partial F_{\mathrm{ph}}}{\partial V}\right)_T. \tag{8}$$

In absence of any internal degree of freedom for the cage guest (i.e. non-magnetic, in particular), one can assume that the ω_0 frequency has negligible temperature dependence below room temperature. The same applies for the lattice of cages represented by the frequency Ω_0. We shall consider that these two characteristic frequencies depend only on the volume V, which, in turn, also applies for the normal modes $\omega_\mu(\mathbf{q})$. In these conditions, the phonon pressure exerted on the crystal matrix can be expressed as in [20]:

$$P_{\mathrm{ph}}(T,V) = P_0 - 3\hbar\sum_{i=1}^{N}\sum_{\mu=(a,o)}\frac{\mathrm{d}\omega_\mu(\mathbf{q}_i)}{\mathrm{d}V}\frac{1}{\mathrm{e}^{\frac{\hbar\omega_\mu(\mathbf{q}_i)}{k_B T}}-1} \tag{9}$$

where P_0 is the zero temperature phonon pressure. For the small volume changes involved, the volume derivatives of the $\omega_\mu(\mathbf{q})$ frequencies are considered as constants.

2.4. Phonons thermal expansion

Introducing χ_0, the compressibility of the lattice, supposed constant in the temperature ranges of interest, the linear thermal expansion coefficient α_{ph} can be related to the phonon pressure:

$$\alpha_{\mathrm{ph}} = \frac{\chi_0}{3}\left.\frac{\partial P_{\mathrm{ph}}}{\partial T}\right)_V. \tag{10}$$

[3] From equations (9) and (10), the thermal expansion coefficient can be expressed as:

$$\alpha_{\mathrm{ph}}(T) = \frac{\chi_0}{3}\sum_{i=1}^{N}\sum_{\mu=(a,o)}\gamma_\mu(\mathbf{q}_i)\cdot c_\mu(\mathbf{q}_i,T) \tag{11}$$

where, for each mode, are introduced:

- an individual Grüneisen parameter,

$$\gamma_\mu(\mathbf{q}_i) = -\frac{V}{\omega_\mu(\mathbf{q}_i)}\frac{\mathrm{d}\omega_\mu(\mathbf{q}_i)}{\mathrm{d}V} \tag{12}$$

- a contribution to the specific heat per unit volume:

$$c_\mu(\mathbf{q}_i,T) = \frac{3k_B}{V}\left(\frac{\hbar\omega_\mu(\mathbf{q}_i)}{k_B T}\right)^2\frac{\mathrm{e}^{-\frac{\hbar\omega_\mu(\mathbf{q}_i)}{k_B T}}}{\left(1-\mathrm{e}^{-\frac{\hbar\omega_\mu(\mathbf{q}_i)}{k_B T}}\right)^2}. \tag{13}$$

To detail the expression for α_{ph}, one needs to define the volume derivative for all $\omega_\mu(\mathbf{q}_i)$ frequencies. Using the generalized dispersion relations, these derivatives can be related to the frequencies ω_0 and Ω_0. Indeed, for a given mode, the cosine $\cos(2\pi qd)$ from equation (1) is independent of the volume. With respect to an infinitesimal volume variation $\mathrm{d}V$, the following differential, involving the mode of frequency $\omega_{\mathbf{q}}$, has to cancel:

$$d\left[\frac{{\omega_{\mathbf{q}}}^2}{{\Omega_0}^2} + \rho\frac{{\omega_{\mathbf{q}}}^2}{{\Omega_0}^2}\frac{{\omega_0}^2}{{\omega_0}^2-{\omega_{\mathbf{q}}}^2}\right] = 0. \tag{14}$$

This translates into a relation between the differentials of $\omega_{\mathbf{q}}$, ω_0 and Ω_0. Introducing the peak function f_ρ of the reduced frequency $y = \omega_{\mathbf{q}}/\omega_0$, defined for a given mass ratio ρ:

$$f_\rho(y) = \frac{\rho}{(1-y^2)^2+\rho} \tag{15}$$

[3] Note that, if one seeks a value for χ_0, the cubic symmetrized elastic constants C_{11} and C_{12} are more easily found in the literature. We recall that χ_0 can be written as:

$$\chi_0 = \frac{3}{C_{11}+2C_{12}}$$

the partial derivatives of $\omega_{\mathbf{q}}$ read as:

$$\left.\frac{\partial\omega_{\mathbf{q}}}{\partial\omega_0}\right)_{\Omega_0} = f_\rho\left(\frac{\omega_{\mathbf{q}}}{\omega_0}\right)\frac{{\omega_{\mathbf{q}}}^3}{{\omega_0}^3} \tag{16}$$

and

$$\left.\frac{\partial\omega_{\mathbf{q}}}{\partial\Omega_0}\right)_{\omega_0} = \frac{\omega_{\mathbf{q}}}{\Omega_0}\left(1 - f_\rho\left(\frac{\omega_{\mathbf{q}}}{\omega_0}\right)\frac{{\omega_{\mathbf{q}}}^2}{{\omega_0}^2}\right). \tag{17}$$

As changes in ω_0 and Ω_0 are uniquely ascribed to the volume change dV:

$$\begin{aligned}\mathrm{d}\omega_{\mathbf{q}} = & f_\rho\left(\frac{\omega_{\mathbf{q}}}{\omega_0}\right)\frac{\omega_{\mathbf{q}}^3}{{\omega_0}^3}V\frac{\mathrm{d}\omega_0}{\mathrm{d}V}\frac{\mathrm{d}V}{V} + \frac{\omega_{\mathbf{q}}}{\Omega_0}\left(1 - f_\rho\left(\frac{\omega_{\mathbf{q}}}{\omega_0}\right)\frac{{\omega_{\mathbf{q}}}^2}{{\omega_0}^2}\right) \\ & \times V\frac{\mathrm{d}\Omega_0}{\mathrm{d}V}\frac{\mathrm{d}V}{V}.\end{aligned} \tag{18}$$

One can then express the individual Grüneisen parameter of equation (12) as:

$$\begin{aligned}\gamma_\mu(\mathbf{q}_i) = & f_\rho\left(\frac{\omega_\mu(\mathbf{q}_i)}{\omega_0}\right)\frac{\omega_\mu(\mathbf{q}_i)^2}{{\omega_0}^2}\gamma_0 \\ & + \left(1 - f_\rho\left(\frac{\omega_\mu(\mathbf{q}_i)}{\omega_0}\right)\frac{\omega_\mu(\mathbf{q}_i)^2}{{\omega_0}^2}\right)\Gamma_0\end{aligned} \tag{19}$$

where a Grüneisen parameter is introduced for each characteristic frequency,

$$\gamma_0 = -\frac{V}{\omega_0}\frac{\mathrm{d}\omega_0}{\mathrm{d}V} \tag{20}$$

for the natural rattler frequency ω_0 and:

$$\Gamma_0 = -\frac{V}{\Omega_0}\frac{\mathrm{d}\Omega_0}{\mathrm{d}V} \tag{21}$$

for the averaged top frequency Γ_0 of a lattice of empty cages.

Thus, the expression for the thermal expansion linear coefficient:

$$\begin{aligned}\alpha_{\mathrm{ph}}(T) = & \frac{\chi_0}{3}\sum_{i=1}^{N}\sum_{\mu=(a,o)} c_\mu(\mathbf{q}_i, T) \\ & \times\left\{\Gamma_0 + (\gamma_0 - \Gamma_0)f_\rho\left(\frac{\omega_\mu(\mathbf{q}_i)}{\omega_0}\right)\frac{\omega_\mu(\mathbf{q}_i)^2}{{\omega_0}^2}\right\}.\end{aligned} \tag{22}$$

In the expression above, one can identify the phonon contribution to the sample specific-heat C_{ph} and its corresponding Grüneisen contribution to the thermal expansion. There is an additional term, specific to the cage phonons model, proportional to the function D_{ph} of the temperature, also dimensionally a specific heat per unit volume:

$$D_{\mathrm{ph}}(T) = \sum_{i=1}^{N}\sum_{\mu=(a,o)} f_\rho\left(\frac{\omega_\mu(\mathbf{q}_i)}{\omega_0}\right)\frac{\omega_\mu(\mathbf{q}_i)^2}{{\omega_0}^2}c_\mu(\mathbf{q}_i, T). \tag{23}$$

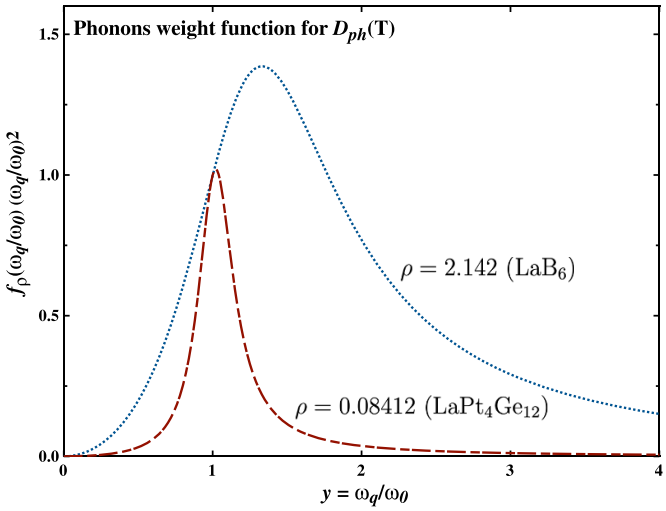

Figure 5. Plots of the weight functions $f_\rho(\frac{\omega_{\mathbf{q}}}{\omega_0})\frac{{\omega_{\mathbf{q}}}^2}{{\omega_0}^2}$, for LaB_6 and $LaPt_4Ge_{12}$, active in the D_{ph} term of the thermal expansion. These two examples are drastically different in terms of the mass ratio ρ, which defines the width of the f_ρ function, with a heavy guest for LaB_6 against a heavy cage for $LaPt_4Ge_{12}$.

As shown in figure 5, the weight function $f_\rho(\frac{\omega_{\mathbf{q}}}{\omega_0})\frac{{\omega_{\mathbf{q}}}^2}{{\omega_0}^2}$ increases the influence of modes with frequencies close to ω_0. In approximative terms, D_{ph} can be considered as the specific heat from modes belonging to the flattened phonon branches around ω_0 (i.e. similar to a Einstein model specific heat). The expression for the phonons thermal expansion coefficient then reads as:

$$\alpha_{\mathrm{ph}}(T) = \frac{\chi_0\,\Gamma_0}{3}\left\{C_{\mathrm{ph}}(T) + \left(1 - \frac{\gamma_0}{\Gamma_0}\right)D_{\mathrm{ph}}(T)\right\} \tag{24}$$

where C_{ph} is the phonons specific heat and D_{ph} the just above discussed flattened branches 'specific heat'. Equation (24) shows that the phonons' model we use is not consistent with the Grüneisen rule. This is no surprise, as the model is based on two frequency parameters, ω_0 and Ω_0. As soon as these frequencies differ in their volume relative derivatives (i.e. $\gamma_0 \neq \Gamma_0$), D_{ph} interferes in the 'proportionality' between α_{ph} and C_{ph}. Instead of a constant parameter, one can introduce an effective Grüneisen function $\gamma_{\mathrm{eff}}(T)$ that reads as:

$$\gamma_{\mathrm{eff}}(T) = \Gamma_0\left\{1 + \left(1 - \frac{\gamma_0}{\Gamma_0}\right)\frac{D_{\mathrm{ph}}(T)}{C_{\mathrm{ph}}(T)}\right\} \tag{25}$$

As the physical contexts underlying the two types of vibrations, those of the guest inside the cage and those of the cage within its lattice, are quite distinct, γ_0 and Γ_0, are unlikely to be identical. The latter case is more similar to simple lattices discussed in the literature, where typical values for metals approach 2 [21]. As regards γ_0, the crudest, non-harmonic, approach is that of a box potential that would yield $\gamma_0 = \frac{2}{3}$. Thus, there is no *a priori* reason to ignore the contribution of the ratio $D_{\mathrm{ph}}(T)/C_{\mathrm{ph}}(T)$ to $\gamma_{\mathrm{eff}}(T)$. This ratio and its temperature behaviour depend only on ω_0, Ω_0 and the mass ratio ρ.

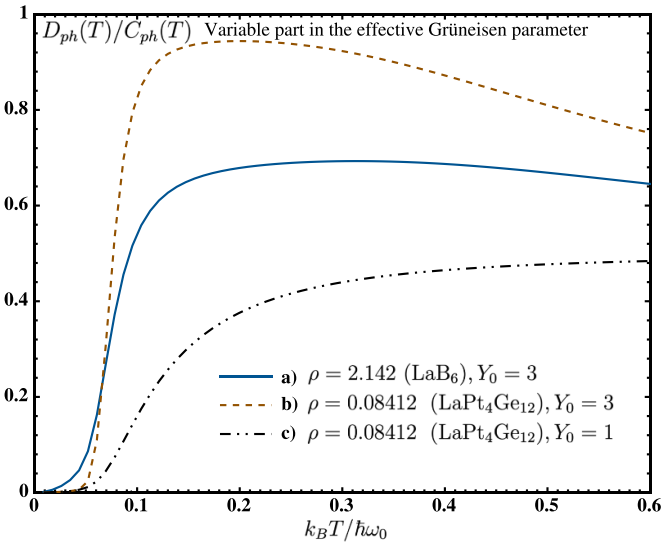

Figure 6. Plots of the ratios $D_{\rm ph}(T)/C_{\rm ph}(T)$, as functions of the reduced temperature $k_{\rm B}T/\hbar\omega_0$, for the same (a), (b) and (c) examples as in figures 2 and 4. These ratios define the variable part in the $\gamma_{\rm eff}(T)$ 'Grüneisen' function, i.e. the deviation from the Grüneisen rule.

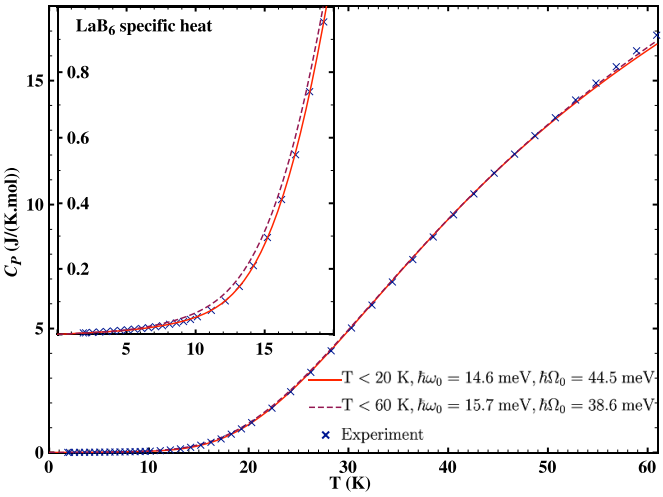

Figure 7. Specific heat data for LaB_6 (crosses). The inset details the low temperature range. The lines are least squares fits using the two frequencies ω_0 and Ω_0 model. The continuous line is a fit to the experimental data for temperatures below 20 K, whereas the doted line is a fit to the full set of data, up to 60 K. The respective, optimized values for ω_0 and Ω_0, are displayed in the legend. The value $\gamma_{\rm e} = 2.3$ mJ $({\rm K}^2.{\rm mol})^{-1}$ for the electronic contribution coefficient to the specific heat is not adjusted (see text).

It can be computed for the examples of figures 2 and 4. The curves on figure 6 show two distinct regimes, the low-temperature Grüneisen rule breaking down at temperatures as low as $T \approx 0.05\ \hbar\omega_0/k_{\rm B}$. In this low temperature regime the Grüneisen parameter identifies with Γ_0: the acoustic branch of the lattice of cages is dominant in the phonons' thermal expansion, drawing a parallel with the Debye approximation for the specific heat. Above $T \approx 0.1\ \hbar\omega_0/k_{\rm B}$, the influence of the Einstein-like flattened phonon branches, related to the rare-earth vibration, becomes evident: after a steep increase, the $D_{\rm ph}(T)/C_{\rm ph}(T)$ ratio stabilizes, leading to a new, nearly constant Grüneisen 'parameter' at intermediate temperatures. This plateau in $D_{\rm ph}(T)/C_{\rm ph}(T)$ is more pronounced when there is a large gap between the two phonon branches (example *a*, with the mass ratio of LaB_6). Since it depends on the unknown difference $\Gamma_0 - \gamma_0$, at this stage, the sign and amplitude of the step in $\gamma_{\rm eff}(T)$ cannot be predicted.

3. Experiments

3.1. Samples

The LaB_6 samples used are single crystals grown at the Frantsevich Institute in Kyiv. The synthesis process is detailed in the supplementary material of [22]. From the zone melting processed rod, a single crystalline platelet was cut with the larger face perpendicular to a twofold axis. This sample was used for the thermal expansion measurements, its diagonal of 6.02 mm length, also along a twofold direction, being the one sensed in the apparatus. For the specific heat measurement, a much smaller sample from the same batch was used, with a mass $m = 6$ mg.

The polycrystalline sample of $LaPt_4Ge_{12}$ was prepared at the Néel Institute, by first melting stoichiometric amounts of the three elements in a cold crucible under an argon atmosphere. Then, to complete the skutterudite phase formation, the ingot was sealed in an evacuated quartz tube and annealed at 780° C for 10 d. Powder x-ray diffraction revealed that the annealed sample was free of parasitic phases, with the x-ray pattern consistent with the filled skutterudite phase. A piece of this ingot, with a sensed length of 5.98 mm, was used for thermal expansion measurements. From the same ingot, a much smaller piece weighing $m = 6.05$ mg was detached for the specific heat measurements.

3.2. Specific heat measurements

The specific heat measurements were performed using the relaxation technique in an automated [23] commercial Quantum Design PPMS system. The thermal coupling between the sample and the setup platform was improved by use of Apiezon N grease, which is accounted for thanks to the addenda measurements. For both the LaB_6 and $LaPt_4Ge_{12}$ sample, the default two time constants fitting of the relaxation process, was used. In order to avoid the anomaly resulting from the superconducting transition in $LaPt_4Ge_{12}$ at $T_{\rm C} = 8.3$ K [9], the specific heat was measured under a 1.2 T applied magnetic field. The measurements for LaB_6 and $LaPt_4Ge_{12}$ are respectively shown in figures 7 and 8.

3.3. Thermal expansion measurements

3.3.1. Use of a magnetostriction setup. The thermal expansion was measured using the in-house developed magnetostriction setup of the Institut Néel. This system consists of a capacitance cell machined from a copper–beryllium alloy,

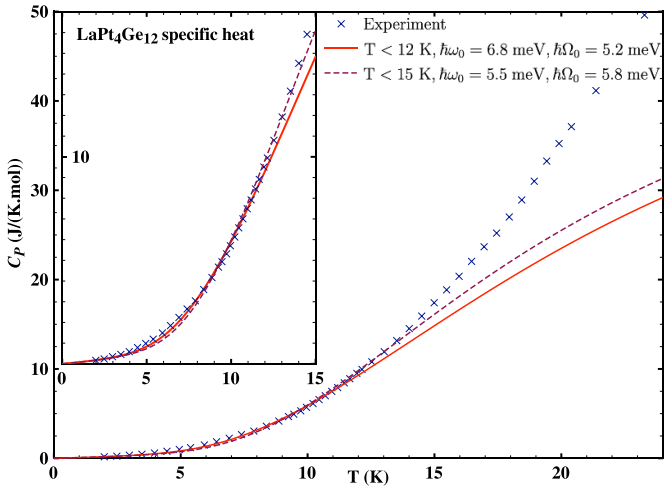

Figure 8. Specific heat measurements for $LaPt_4Ge_{12}$ under a 1.2 T applied magnetic field, in order to suppress the superconducting transition at $T_C = 8.3$ K, with low temperature detail in the inset. The lines are least squares fits using the two frequencies ω_0 and Ω_0 model and fixed value $\gamma_e = 80$ mJ $(K^2{\cdot}mol)^{-1}$ coefficient for the electronic contribution to the specific heat. The continuous line is a fit to the experimental data for temperatures below 12 K while the doted line extends the range to 15 K. The respective optimized values for ω_0 and Ω_0 are displayed in the legend.

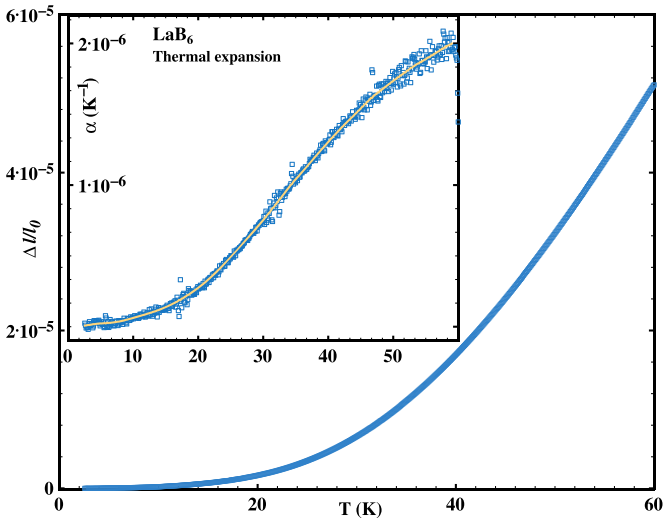

Figure 9. Thermal expansion of LaB_6, as the relative change in length with respect to l_0 at 2.5 K, measured on a single crystal with a capacitance dilatometer while cooling down from 60 K to 2.5 K. The inset gives the linear thermal expansion coefficient α, as a numerical derivative (scattered points) and with applied low-pass filtering (light color, solid line, for a filtering constant $\tau = 1.5$ (K).

housed in a helium flux cryostat equipped with a superconducting magnet that provides a horizontal magnetic field up to 6 T. The cell can be rotated along a vertical axis, allowing for length measurements both along and perpendicular to the applied magnetic field, within a temperature range of 2–300 K. The sample is glued on a Cu–Be sample holder with Stycast 2850FT, the other end being free but elastically pressed against the moving electrode. The cell and associated capacitance bridge can detect changes in length as small as 1 Å, enabling the system to sense relative expansions down to 10^{-7} for samples of a few millimeters in length. The main issue, in using this system for thermal expansion measurement, is that it was originally designed for field variations at constant temperature. For variable temperature measurements, corrections must be made for the cell's thermal hysteresis. This is done by measuring a reference sample, a sphere made of the same copper–beryllium alloy as the cell, following a temperature cycle identical in rate and interval to that applied to the investigated sample. Another effect of temperature variation, which becomes significant below 5 K, is the change in the low-pressure helium dielectric constant. From the reference sample measurement, a capacitance correction is applied based on the Clausius–Mossotti relation.

3.3.2. Linear thermal expansion coefficient. To obtain the temperature variation of the linear thermal expansion coefficient $\alpha(T)$ from the sample length $l(T)$, one has to resort to a numerical approximation of the analytical relation:

$$\alpha(T) = \frac{1}{l}\left.\frac{\partial l}{\partial T}\right)_P \qquad (26)$$

The linear thermal expansion coefficient, obtained from a numerical differentiation, is typically noisy when small temperature increments cause length changes at the limit of the apparatus sensitivity. An added difficulty is the occasional slip of the sample's contact point on the moving electrode, that yields parasitic peaks. To mitigate this dispersion in the data, a subsequent filtering can be applied. The filtering used here is a numerical analog to an RC low-pass filter, the input being the numerical derivative as function of the temperature. Instead of a time constant, a value for a temperature constant τ is visually adjusted in order to dampen the abrupt changes that develop on smaller temperature scales. Such a filtering introduces a delay in the signal with respect to the temperature evolution. This delay is essentially cancelled by successively applying the filtering both up and down the temperature list, the two resulting outputs being then averaged. As the principle is the numerical solving of a first-order differential equation, one has to carefully choose the initial values of the output in both directions. In our case, these initial values are obtained by minimizing a chi-squared reflecting the distance between the filtered output and the noisy input.

Figure 9 shows the measurement relative change in length for LaB_6, as obtained under zero magnetic field and decreasing temperature between 60 K and 2.5 K at a rate of 0.2 K min^{-1}. In the inset, the linear thermal expansion coefficient is displayed, as obtained from simple direct numerical differentiation (scattered points) and using a low-pass filter for a constant $\tau = 1.5$ K (continuous line).

The measurements for $LaPt_4Ge_{12}$ are displayed on figure 10. The relative change in length $\Delta l/l$ is obtained from measurements at a small rate of 0.05 K min^{-1} from 2.5 K to 120 K, in zero magnetic field, in both cooling and heating conditions. The data from the two temperature variations

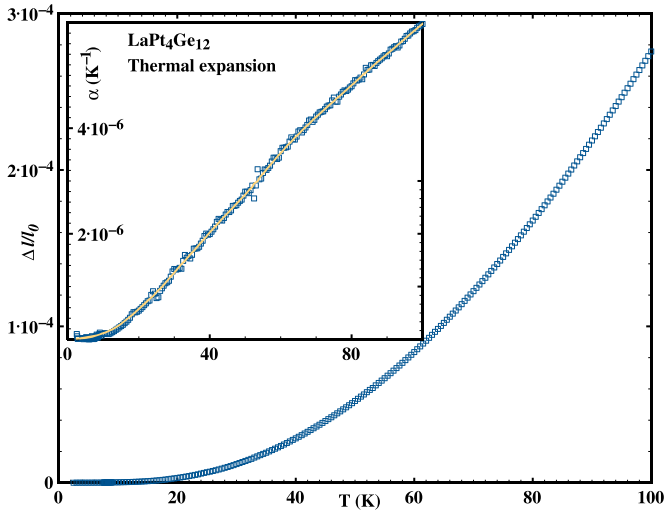

Figure 10. Thermal expansion of $LaPt_4Ge_{12}$, as the relative change in length with respect to the lowest temperature length l_0, measured on a polycrystalline sample with a capacitance dilatometer. The data below 9 K is measured under an applied magnetic field of 1.2 T to suppress the superconducting anomaly. Above 9 K, the measurements are for zero field. The inset gives the linear thermal expansion coefficient α, as a numerical derivative (scattered open squares) and with applied low-pass filtering (solid line, filtering constant $\tau = 3$ K).

were then averaged as an additional mean for compensating the cell hysteresis. As this paper focuses on the effect of the low energy phonons, the temperature range of the figure is restricted to values below 100 K. Also, $LaPt_4Ge_{12}$ undergoing a superconducting transition at $T_C = 8.3$ K, with a slight volume anomaly, the data below 9 K is replaced by measurements done under an applied magnetic field of 1.2 T. The inset of figure 10 shows the linear thermal expansion coefficient temperature variation, from direct numerical differentiation and subsequent low-pass filtering (continuous line) with a filtering constant $\tau = 3$ K.

4. Analysis

4.1. Specific heat

The two dominant contributions to the specific of a non-magnetic, metallic compound are:

- the conduction electrons specific heat, here reduced to its linear, low temperature term: $C_e(T) = \gamma_e T$, with γ_e a constant characteristic of the system.
- the phonon contribution: $C_{ph}(T)$ which, for calculation, requires some model for the phonon dispersion curves.

$C_{ph}(T)$ is here computed using the two frequencies, two branches, generalized dispersion curves for cage compounds. Using equation (6) and an appropriate sampling of the first Brillouin zone, the $C_{ph}(T)$ specific heat can be numerically calculated as a function of temperature for any given pair of frequency values (ω_0, Ω_0). As regards the γ_e electronic constant, it can be directly determined from the specific heat experimental data $C_p(T)$. Here, the values used are obtained from the 0 K extrapolation of the plot of C_p/T as function of T^2. Once γ_e is defined, values for ω_0 and Ω_0 can de retrieved from a least squares fit to the experimental data.

4.1.1. LaB_6. Figure 7 shows, as functions of the temperature, the results of calculations superimposed with the specific heat data. The computed values include an electronic contribution for $\gamma_e = 2.3 \pm 0.1$ mJ $(K^2 \cdot mol)^{-1}$, deduced from the plot of C_P/T against T^2. The mass ratio $\rho = 2.142$ corresponds to a lanthanum ion inside a cage of natural boron. To expedite the calculation of C_{ph} (equation (6)) during the fitting process, the number of samples in the representative volume of the first Brillouin zone of the cubic lattice was limited to 364, which is sufficient to approach the large-number limit, without noticeable effects at the graph's scale. The choice of the temperature range, used for the optimization of the ω_0 and Ω_0 values, is crucial. Clearly, the model, based on only two phonon branches, treating the boron cage as a single object, cannot hold at higher temperatures, where it would violate the *Dulong et Petit* law. In figure 7, two least squares refinements are displayed, one restricted to data for temperatures below 20 K (full line), the other generalized to the full set, up to 60 K (dashed line). It is apparent that, in both cases, the model struggles to describe the experiment above 50 K. For the extended set of temperatures, the description above 50 K is marginally improved at the expense of accuracy in the low temperature range (see the inset).

The best fit below 50 K is obtained for the low temperature data set ($T < 20$ K), which aligns with the model's expected limitations at higher temperatures. The refined values are $\hbar\omega_0 = 14.6$ meV and $\hbar\Omega_0 = 44.5$ meV, resulting in a ratio $Y_0 = \Omega_0/\omega_0 = 3.05$ close to the value 3 used in the *a*) example in figures 2, 4 and 6. The value for $\hbar\omega_0$ slightly exceeds the inelastic neutron scattering [7, 16] investigation, which points to a value of approximately 13.5 meV. From this LaB_6 example, it can be concluded that the model accurately describes the phonon specific heat up to one-third of $\hbar\omega_0/k_B$, i.e. about 50 K. Above this limit, higher energy phonon branches become influential, increasing the specific heat relative to the two frequencies model. In rare-earth hexaborides, at least, this limitation is inconsequential, as the relevant magnetic phenomena typically occur below 30 K. For instance, in CeB_6, this phonon description is effective in defining the temperature dependence of the magnetic entropy below 50 K [7].

4.1.2. $LaPt_4Ge_{12}$. The preliminary analysis, from the plot of C_P/T as function of T^2, yields a value for the electronic contribution to the specific heat: $\gamma_e = 80 \pm 6$ mJ $(K^2 \cdot mol)^{-1}$, consistent with earlier determinations [9]. The massive cage results in a small mass ratio $\rho = 0.08412$. Subsequently, one can proceed with the fit of the experimental data by adjusting the values of ω_0 and Ω_0, using equation (6). The calculations in

figure 8 are performed for 650 samples within the representative volume of the body centered first Brillouin zone. The fitting procedure is applied to data from reduced low-temperature intervals, either below 15 K (dotted line) or below 12 K (solid line). Indeed, to obtain a reasonable fit, it is necessary to significantly lower the upper temperature limit. It appears that low energy modes, unaccounted for in our two-frequency description, become influential at temperatures as low as 15 K, causing the experimental data to rapidly exceed the calculated values. The fits shown in figure 8 yield similar values for ω_0 and Ω_0 (i.e. $Y_0 = \Omega_0/\omega_0 \approx 1$), suggesting a flattened optical branch with a high density of modes just above ω_0 (see the dispersion curves of example *c* in figures 2 and 4). However, when confronted with the inelastic neutron scattering results [19], the fitted values are not satisfactory. The lowest energy phonon peak in the spectra is observed around 7.5 meV, while the specific heat fits in figure 8 would correspond to a peak slightly above 5 meV. The same inelastic scattering data reveals the proximity of phonon branches, unaccounted in the model, with the closest peak at about 15.5 meV. Below 20 K, the fit compensates for these missing contributions by lowering the energies of the two included branches.

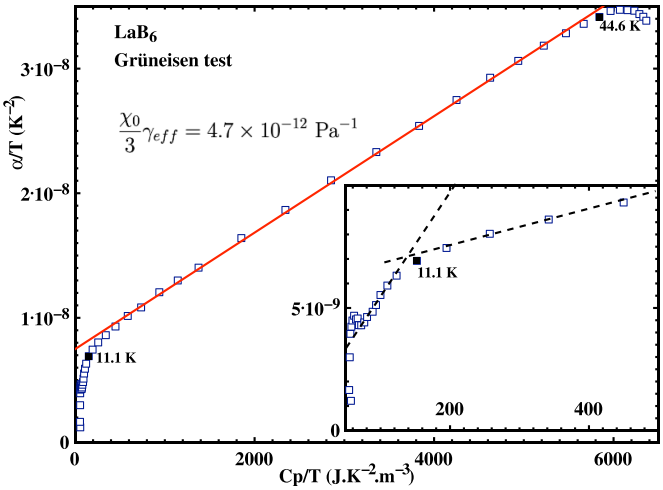

Figure 11. Test of the Grüneisen rule for LaB_6 by plotting α/T, where α is the linear thermal expansion coefficient for LaB_6, againts C_p/T, C_p being the measured specific heat of LaB_6. For each temperature in the specific heat data a corresponding α value is identified using the low-pass filtered α curve (solid line in the inset of figure 9). Between 12 K and 45 K (see black squares), a nearly linear relation is observed that yields $\chi_0\gamma_{\text{eff}}/3 = 4.7 \times 10^{-12}$ Pa^{-1} for LaB_6. The inset highlights the low temperature region, with dashed lines pointing to a crossover at about 11 K.

4.2. *Testing the Grüneisen rule*

An experimental assessment of the Grüneisen rule requires, over a given temperature range, to define the ratio between the thermal expansion coefficient, $\alpha(T)$, and the specific heat $C_P(T)$. Measurements of these physical quantities for metals include contributions from the conduction electrons, whereas the present work focuses on the phonon contributions only. Since the conduction electrons terms, both for the thermal expansion and specific heat, are expected to vary linearly with the temperature across a broad range, more relevant quantities for an illustrative graph are $\alpha(T)/T$ and $C_P(T)/T$. The electronic contributions are thus reduced to constants and visually neutralized in the temperature evolution. In the following, the analysed plots are those of $\alpha(T)/T$ as function of $C_P(T)/T$. If the Grüneisen function γ_{eff}, introduced in equation (25), is relatively constant over an extended temperature range, the graph will display a corresponding strait line. The slope of this line, that averages γ_{eff}, identifies with a local Grüneisen parameter. Such plots require, at each temperature, experimental determinations for both $\alpha(T)$ and $C_P(T)$. Since the thermal expansion and specific heat data were collected separately, for different sets of temperatures, an extrapolation is needed. For each temperature in the specific heat dataset, a corresponding α value is identified using the low-pass filtered α curve (see paragraph 3.3.2). Additionally, the specific heat unit is converted from J·K^{-1}· mol^{-1}to J·K^{-1}· mol^{-1}, so that a slope in the graph has the dimension of a compressibility, i.e. the inverse of a pressure.

4.2.1. LaB_6. Figure 11 shows the test graph of the phonon Grüneisen rule for LaB_6. Between 13 and 45 K, one observes a nearly linear relationship between $\alpha(T)/T$ and $C_P(T)/T$. According to equations (24) and (25), the slope of this linear region provides a value for the average of $\chi_0\gamma_{\text{eff}}(T)/3$ in this temperature range. The compressibility χ_0 at low temperature can be deduced from published elastic constants measurements [24], yielding: $\chi_0 = 5.32 \pm 0.06 \times 10^{-12}$ Pa^{-1}. An estimate of γ_{eff}, the average of the Grüneisen function over the linear region, is thus obtained as: $\gamma_{\text{eff}} = 2.7$.

Below 11 K, another regime is observed (see inset of figure 11), with a steeper slope, indicating a larger γ_{eff} value. Although this region also appears fairly linear, caution is required as the dilatometer approaches its sensitivity limits below 8 K, resulting in increased relative scattering of α values, particularly below 5 K (see figure 9). Nevertheless, it can be concluded that $\gamma_{\text{eff}}(T)$ is significantly larger below 11 K than above. According to equation (25), this implies that γ_0 is larger than Γ_0 (both should be positive), suggesting that the cage oscillator is more sensitive to volume changes than the lattice of cages. The crossover temperature between the two low-temperature regions is around $T_{\text{co}} = 11$ K (see inset of figure 11). With parameters close to those of the specific heat fit, the *a*) example in figure 6 predicts a step in γ_{eff} at $k_B T_{\text{co}}/\hbar\omega_0 \approx 0.07$. This yields $\hbar\omega_0 \approx 13.5$ meV, a value in striking agreement with neutron spectroscopy and specific heat determinations.

Above 45 K, no Grüneisen rule holds: additional phonon branches start to interfere, as observed in the specific heat data fits (figure 7).

4.2.2. $LaPt_4Ge_{12}$. Figure 12 illustrates the test of the Grüneisen rule for phonons in $LaPt_4Ge_{12}$. The filtered thermal expansion data used for the plot were restricted to temperatures above the superconducting transition, to avoid artifacts

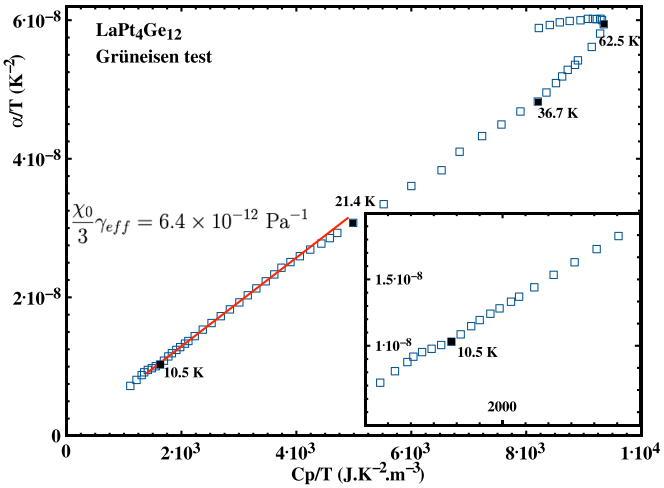

Figure 12. Test of the Grüneisen rule for $LaPt_4Ge_{12}$ by plotting α/T, where α is the linear thermal expansion coefficient for $LaPt_4Ge_{12}$, against C_p/T. For each temperature in the specific heat data set a corresponding α value is interpolated using the low-pass filtered data, limited to values above the superconducting transition. The inset highlights the low temperature range and the black squares mark particular temperatures. Between 11 K and 21 K, a linear relation is observed that yields $\chi_0\gamma_{\text{eff}}/3 = 6.4 \times 10^{-12}$ Pa^{-1} for $LaPt_4Ge_{12}$.

resulting from the merging of different data sets (the data in figure 10 are composite, combining zero-field measurements with data collected below 9 K under a magnetic field of 1.2 T). The graph reveals at least five distinct regions, separated by black squares. The two-frequency model can only account for the lower temperature range, where, between 11 and 21 K, an approximate Grüneisen rule is observed. Within this range, the average $\chi_0\gamma_{\text{eff}}/3$ is estimated to be 6.4×10^{-12} Pa^{-1}. Due to the lack of available compressibility data for χ_0, no value can be derived for the averaged Grüneisen function γ_{eff}. In the lower temperature region, below the crossover at $T_{\text{co}} = 10.5$ K (inset of figure 12), the slope decreases, which, unlike in the LaB_6 case, suggests a γ_0 value smaller than Γ_0, indicating a reduced influence of the cage oscillator on the thermal expansion in $LaPt_4Ge_{12}$. From the specific heat analysis, it was found that, among the treated dispersion examples, $LaPt_4Ge_{12}$ was closer to case c), with $Y_0 \approx 1$. In figure 6, the step for case c) is rather smooth, centered around $k_B T_{\text{co}}/\hbar\omega_0 \approx 0.12$. Within the two-frequency model, this allows to estimate $\hbar\omega_0 \approx$ 7.5 meV, a value larger than those derived from the specific heat fits, but consistent with the neutron spectroscopy data.

At higher temperatures, one can identify other quasi-linear regimes. It is tempting to speculate that these changes in the $\chi_0\gamma_{\text{eff}}/3$ slope are due to the successive interference of higher energy flattened phonon branches. At about 62 K, there is a turning point in the plot, showing that both C_P/T and α/T decrease above this temperature.

5. Discussion

This study clarifies the limits of the two-frequency model for rare-earth cage systems. In the case of LaB_6, the light and rigid lattice of boron cages isolates the two lowest phonon branches, allowing for an accurate description of the specific heat, up to temperatures equivalent to one-third of the natural frequency, ω_0, of the Lanthanum guest. This is in contrast with the filled skuterrudite $LaPt_4Ge_{12}$. By analogy with LaB_6, one might expect an accurate specific heat description up to 30 K, yet discrepancies emerge as early as 15 K. This is due to the model's neglect of vibrations within the massive Pt_4Ge_{12} cage, at frequencies close to that of the lanthanum guest atom, as revealed by the inelastic neutron scattering spectra. A minimal extension of the two-frequency model would be to treat the Ge_{12} and Pt_4 components of the cage as separate entities rather than a single mass unit. This would add an optical branch (for each polarization) at the cost of, at least, one additional frequency parameter and its Grüneisen counterpart. In this process, one would sacrifice the analytical simplicity of the dispersion relations and diminish its advantages over a fully numerical approach, such as the Density Functional Theory.

These same analytical relations enable the extension of the two-frequency model to describe, within the quasi-harmonic approximation, the thermal expansion. This description involves two separate Grüneisen parameters, γ_0 and Γ_0, respectively related to the characteristic frequencies ω_0 and Ω_0. Under these conditions, the system cannot conform to a simple Grüneisen rule. Instead, the model predicts two successive Grüneisen regimes:

- at low temperatures, an approximate Grüneisen rule is followed, dominated by low-energy acoustic phonons,
- at temperatures greater than one-tenth of $\hbar\omega_0/k_B$, the influence of the flattened phonon branches become significant, leading to a second approximate Grüneisen rule.

In place of a single Grüneisen parameter, it is then natural to define a Grüneisen function of the temperature, as the ratio between the thermal expansion coefficient and the specific heat of phonons. This function is sensitive to changes in the distribution of vibrational modes across multiple phonon branches. By combining experimental data for specific heat and thermal expansion, appropriate plots can be generated to identify distinct temperature regions, highlighting changes in the Grüneisen function. In the examples of LaB_6 and $LaPt_4Ge_{12}$, these plots confirm the expected regime transitions, moreover at temperatures that match the model's quantitative predictions.

From an experimental standpoint, the main difficulty arrises from the limited sensitivity of our dilatometer. Below 10 K, changes in the sample length are difficult to detect, leading to large scatter in the experimental data. This hampers the graphical definition of the lower temperature regime, related to the cage lattice Grüneisen parameter Γ_0. Consequently, a quantitative determination of Γ_0 and, subsequently, γ_0, is difficult. Furthermore, these determinations require complementary experimental data on low-temperature compressibility, which are lacking in the $LaPt_4Ge_{12}$ case.

Nevertheless, the two-frequency model and its application to the investigation of the non-magnetic LaB_6 and $LaPt_4Ge_{12}$,

provide a valuable insights into the thermal expansion mechanism in cage compounds. This understanding will help clarify the role of the orbital and spin degrees of freedom in systems where the lanthanum is replaced by a magnetic ion.

Data availability statement

All data that support the findings of this study are included within the article (and any supplementary files).

ORCID iDs

Mehdi Amara https://orcid.org/0000-0002-2024-6492
Natalya Yu Shitsevalova https://orcid.org/0000-0001-9967-3990

References

[1] Keppens V, Mandrus D, Sales B C, Chakoumakos B C, Dai P, Coldea R, Maple M B, Gajewski D A, Freeman E J and Bennington S 1998 *Nature* **395** 876–8
[2] Sales B, Mandrus D and Williams R K 1996 *Science* **272** 1325–8
[3] Amara M, Luca S, Galéra R M, Givord F, Detlefs C and Kunii S 2005 *Phys. Rev.* B **72** 64447
[4] Amara M, Galéra R M, Aviani I and Givord F 2010 *Phys. Rev.* B **82** 224411
[5] Walker H C, McEwen K A, McMorrow D F, Bleckmann M, Park J G, Lee S, Iga F and Mannix D 2009 *Phys. Rev.* B **79** 054402
[6] Amara M 2019 *Phys. Rev.* B **99** 174405
[7] Amara M, Opagiste C and Galéra R M 2020 *Phys. Rev.* B **101** 094411
[8] Grüneisen E 1908 *Ann. Phys., Lpz.* **331** 211–6
[9] Gumeniuk R, Schnelle W, Rosner H, Nicklas M, Leithe-Jasper A and Grin Y 2008 *Phys. Rev. Lett.* **100** 017002
[10] Gumeniuk R, Kvashnina K O, Schnelle W, Nicklas M, Borrmann H, Rosner H, Skourski Y, Tsirlin A A, Leithe-Jasper A and Grin Y 2011 *J. Phys.: Condens. Matter* **23** 465601
[11] Jeitschko W and Braun D 1977 *Acta Crystallogr.* B **33** 3401–6
[12] Bauer E D, Frederick N A, Ho P C, Zapf V S and Maple M B 2002 *Phys. Rev.* B **65** 100506
[13] Iwasa K, Hao L, Kuwahara K, Kohgi M, Saha S R, Sugawara H, Aoki Y, Sato H, Tayama T and Sakakibara T 2005 *Phys. Rev.* B **72** 024414
[14] Keller L, Fischer P, Herrmannsdörfer T, Dönni A, Sugawara H, Matsuda T, Abe K, Aoki Y and Sato H 2001 *J. Alloys Compd.* **323–324** 516–9
[15] Mandrus D, Sales B and Jin R 2001 *Phys. Rev.* B **64** 12302
[16] Smith H G, Dolling G, Kunii S, Kasaya M, Liu B, Takegahara K, Kasuya T and Goto T 1985 *Solid State Commun.* **53** 15–19
[17] Lee C H, Hase I, Sugawara H, Yoshizawa H and Sato H 2006 *J. Phys. Soc. Japan* **75** 123602
[18] Marek Koza M, Adroja D, Takeda N, Henkie Z and Cichorek T 2013 *J. Phys. Soc. Japan* **82** 114607
[19] Galéra R M, Opagiste C, Amara M, Zbiri M and Rols S 2015 *J. Phys.: Conf. Ser.* **592** 012011
[20] Ashcroft N W and Mermin N D 1976 *Solid State Physics* (Holt-Saunders)
[21] White G K and Mendelssohn K A G 1965 *Proc. R. Soc.* A **286** 204–17
[22] Azarevich A N *et al* 2024 *JETP Lett.* **119** 934–41
[23] Hwang J S, Lin K J and Tien C 1997 *Rev. Sci. Instrum.* **68** 94–101
[24] Nakamura S, Goto T, Kunii S, Iwashita K and Tamaki A 1994 *J. Phys. Soc. Japan* **63** 623–36